Composites Science and Technology 270 (2025) 111269

Contents lists available at ScienceDirect

Composites Science and Technology

journal homepage: www.elsevier.com/locate/compscitech

Self-healing interfaces in fiber reinforced polymers: Computational modeling

Yulin Sun [a,*], Laura Simonini [b], Chen Xing [c], Leon Mishnaevsky Jr. [a,*]

[a] Department of Wind and Energy Systems, Technical University of Denmark, Roskilde, 4000, Denmark
[b] Department of Industrial Engineering, University of Trento, Trento, 38123, Italy
[c] Independent Scientist, Roskilde, 4000, Denmark

ARTICLE INFO

Keywords:
Self-healing
Interface
Thermomechanical
Traction–separation law
Friction

ABSTRACT

Fiber-matrix interfaces play a critical role in determining the durability of composite structures. The prospect of developing self-healing interfaces could pave the way for significantly extending their service life. In this study, we investigate the self-healing potential of nanostructured layers at interfaces of epoxy/carbon fiber composites. A three-dimensional thermomechanical model of epoxy/carbon fiber composites with a self-healing nanostructured polycaprolactone (PCL) layer at fiber–matrix interfaces is developed. A fully coupled thermal-stress procedure is established to simulate the healing process of interfaces. To better capture the realistic interfacial properties of this material, both residual stress and surface roughness are considered. Temperature-dependent material properties are included in the model, and heat generation during PCL recrystallization is analyzed. The proposed model is validated by comparing numerical predictions with the microbond testing data of this novel composite material. Numerical results reveal that surface roughness enhances interfacial strength while residual stresses reduce it. Furthermore, the healing process not only restores the interface bonds but also reduces thermal residual stress in the healed material. This study provides valuable insights into leveraging self-healing interfaces to enhance the durability of composite structures.

1. Introduction

Fiber-reinforced polymers (FRPs) are widely used for structural applications due to their high strength-to-weight ratios and exceptional durability [1,2]. Wind turbine blades represent a special case, where large moving composite structures should function for several decades, while their maintenance and repair are almost prohibitively expensive [3,4]. Our earlier work [5] revealed that all critical wind blade failure mechanisms start from interfaces. For instance, structural collapse and buckling of a blade are often the results of debonding of outer skin/shell. Ply drop failure of wind turbine blades is caused by delamination and interface debonding, while failure of trailing edges and other adhesive joints is caused by adhesive layer degradation [5]. Therefore, the strong, damage-resistant interface determines the lifetime of wind turbine blades. By preventing interface failure, one can extend the wind turbine blade lifetime.

A promising approach to prevent or counteract the interface degradation of composites is the development of FRPs with self-healing interfaces. Such self-healing capabilities would allow for autonomous damage repair, extend service life, and significantly reduce maintenance costs. In recent decades, various self-healing mechanisms have been reported for polymer composites, which can generally be categorized into two main categories [6]: extrinsic and intrinsic self-healing mechanisms. Extrinsic self-healing, also known as autonomous self-healing, involves the use of a prefilled healing agent within containers embedded in the matrix to repair damage [7,8], while intrinsic self-healing relies on the chemical bonds of the matrix itself to restructure in the presence of external stimuli such as UV light, heat, or chemicals [9–11]. Extrinsic systems, in the form of capsules or vascular systems, have been incorporated into FRPs; however, the majority of research on capsule-based healing systems has demonstrated only one single healing occurrence [12,13]. In contrast, intrinsic healing material is designed with inherent repeatable repair abilities after damage, which do not depend on external healing agents and catalyst, allowing for multiple healing cycles over time [14,15].

To impart remendability at interfaces of FRPs, Peterson et al. [16] demonstrates the use of a reversible Diels–Alder reaction at the polymer–glass interface with an overall average of 41% repeatable healing efficiency. Zhang et al. [17] proposed a simple and efficient surface treatment method to introduce thermally reversible Diels–Alder adducts on carbon fiber surface by a new sizing agent with healing efficiency up to 93.8% for the first healing cycle. Although thermally reversible Diels–Alder bonds can repeatedly repair the damaged interface, the treatment process is cumbersome. Li et al. [18] introduces a self-healing carbon fiber/polyvinyl alcohol (CF/PVA) composite structure

* Corresponding authors.
E-mail addresses: yulins@dtu.dk (Y. Sun), lemi@dtu.dk (L. Mishnaevsky Jr.).

https://doi.org/10.1016/j.compscitech.2025.111269
Received 25 February 2025; Received in revised form 15 April 2025; Accepted 10 June 2025
Available online 23 June 2025

using reversible hydrogen-bonded interactions, achieving a self-healing efficiency of 73.6%. A straightforward self-healing approach [19] entails integrating a thermoplastic polymer, which acts as a thermally activated healing agent, at the interlaminar interface. Upon heating, the thermoplastic polymer melts and facilitates healing. Due to low process complexity and melting temperature (about 60 °C), polycaprolactone (PCL) is a competitive self-healing thermoplastic agent for polymer composites [20–22]; however, its potential as an interfacial self-healable material has not been extensively explored in existing research. Simonini et al. [23] firstly developed a nanostructured PCL-based multifunctional layer in epoxy/carbon fiber (EP/CF) composites. This work will be focused on investigating damage and healing mechanisms of this new composite material based on computational modeling.

In order to evaluate the degree of fiber matrix adhesion, the microbond test [24,25] is widely conducted to achieve interfacial shear strength (IFSS) at the interface of fiber and matrix. The microbond test (also known as micro-debond, microbond pull-out or single-fiber-microbond-pull-out) [26] was developed by Miller et al. [27] as an adaptation of the traditional pull-out test. To improve the resolution of fracture evolution at the interface, Dsouza et al. [28] introduced local strain measurement in the microbond test and analyzed the effects of critical factors on the microbond test in recent studies [29,30]. For a deeper insight into the microbond test results, computational models are required due to their predictability and guidability. Depending on various boundary conditions, simulations can employ a 2D axisymmetric model [31], a quarter 3D model [32], a half 3D model [33], or a full 3D model [34]. Cohesive zone model (CZM) is one of the most widely used to analyze interfacial debonding [25,35], which models the fracture process as a progressive separation of material interfaces rather than an abrupt failure. Although computational models for microbond testing of FRPs are well-established, research efforts directed towards FRPs with a self-healing layer remain limited. Simonini et al. [36] developed a continuous PCL layer on glass fibers and performed a finite element analysis of the interfacial region; however, their computational model does not account for thermal residual stress and surface roughness, which will be investigated in this work.

This work aims to investigate EP/CF composites with a self-healing PCL layer. It was reported that thermosets dominate the FRP market, accounting for around 80% of it [37]. In wind industry, polyester resins initially served as the matrix material for composite wind blades. As wind turbine sizes increased, EP resins replaced polyester and are now the dominant matrix material in wind blade composites [38]. Thus, EP/CF was selected for investigation in our work. Due to low process complexity and melting temperature, PCL is a promising thermoplastic healing agent in FRP [20–22]. In our recent work by Simonini et al. [23], a novel nanostructured PCL-based multifunctional layer in EP/CF composites was developed. PCL nanoparticles were synthesized by solvent-displacement method and subsequently deposited on the CF surface through an electrophoretic deposition method to obtain an intrinsic self-healing interface.

In this study, based on prior experimental findings [23], we develop a thermomechanical model of the EP/CF composite with a self-healing layer, incorporating the effects of both surface roughness and thermal stress. For surface roughness, Coulomb friction is analyzed by using a frictional cohesive contact surface interaction between PCL and epoxy. Besides, the additional frictional stress induced by rough interfaces is addressed by introducing a debond-length-dependent frictional shear stress. To investigate the thermal effects, a fully coupled thermal-stress analysis is conducted accounting for phase change of PCL by using temperature-dependent material properties. The heat energy generated during the healing process is calculated by `HETVAL` subroutine in ABAQUS. The proposed computational model is effectively validated by microbond tests, providing some valuable insights into improving the durability of composite structures by incorporating self-healing interfaces.

The structure of this manuscript is as follows: Section 2 presents the mechanism of EP/CF composites incorporating a healable polycaprolactone (PCL) layer and introduces the microbond test employed to evaluate interfacial properties. Section 3 details the finite element modeling of the geometry and the frictional cohesive interface, along with the thermomechanical model for coupled thermal-stress analysis. In Section 4, the simulation results are presented and analyzed, emphasizing their alignment with experimental observations and the implications for interfacial healing mechanisms. Finally, Section 5 summarizes outcomes, draws conclusions, and suggests paths for future research.

2. Self-healing interface of epoxy/carbon composites

In this section, we first explain the mechanism of the self-healing EP/CF interface and the material employed in Section 2.1 and Section 2.2. Subsequently, the experimental techniques used to evaluate the interfacial mechanical performance are elaborated in Section 2.3 and Section 2.4.

2.1. Intrinsic self-healing mechanism of EP/CF composite with PCL layers

A novel nanostructured PCL-based multifunctional layer in EP/CF composites (as shown in Fig. 1(a)) was first designed and investigated by Simonini et al. [23]. For clarity purposes, Fig. 1(b) schematically illustrates the overall mechanism of the healing process based on experimental observations. When debonding occurs at the interface between epoxy and carbon fibers, the self-healing mechanism can be triggered by external heat. In the experiment, an electric current was applied to the carbon fibers. The Joule heating effect causes the surface temperature of the carbon fibers to rise, which in turn heats the surrounding PCL layers, leading to the melting of PCL. Upon cooling, the debonded interface can be restored through the recrystallization of the PCL layer. It should be noted that, as shown in Fig. 1(a), the PCL layer surface is initially rough, but it becomes smoother after the healing treatment. This phenomenon will be investigated in the computational model.

2.2. Materials and sample preparation

CFs (GV-201 UTFX) were supplied by Angeloni S.r.l. (Venice, Italy) as a unidirectional fabric with an average fiber diameter of 7 μm. A bi-component epoxy system was provided by Elantas Italia S.r.l. (Collecchio, Italy), comprising an epoxy base (EC 157) and an aminic hardener (W 342) in a 100:30 weight ratio. 3-mm PCL pellets (density = 1.1 g/cm^3, molecular weight [M_w] = 80,000 g/mol) were purchased from Polysciences, Inc. (Warrington, PA, USA), functioning as an interfacial self-healing agent. Poly(vinyl alcohol) (PVA, density = 1.2 g/cm^3, M_w = 50,000 g/mol) and polysorbate 80 (Tween® 80, density = 1.1 g/cm^3, pH = 5.5–7.5, Brookfield viscosity 400–620 cps) were used to stabilize PCL nanoparticles, provided by Sigma Aldrich (Saint Louis, MO, USA) as a water-soluble powder and a yellowish viscous liquid, respectively.

Detailed experimental settings have been elaborated in our recent work by Simonini et al. [23]. Briefly, a solvent-displacement method was employed to achieve a PCL-nanoparticle solution with a well dispersion of PCL nanoparticles in water, as outlined in [39]. Electrophoretic deposition (EPD) was utilized to deposit PCL nanoparticles on CFs surface to obtain an intrinsic self-healing layer. A micropipette was used to deposit EP microdroplets onto single CF fibers that are glued to a paper frame. These EP droplets were cured for 8 h at room temperature followed by 40 h at 50 °C, which is below the melting temperature of PCL (60 °C) to retain the pristine morphology of the nanoparticles.

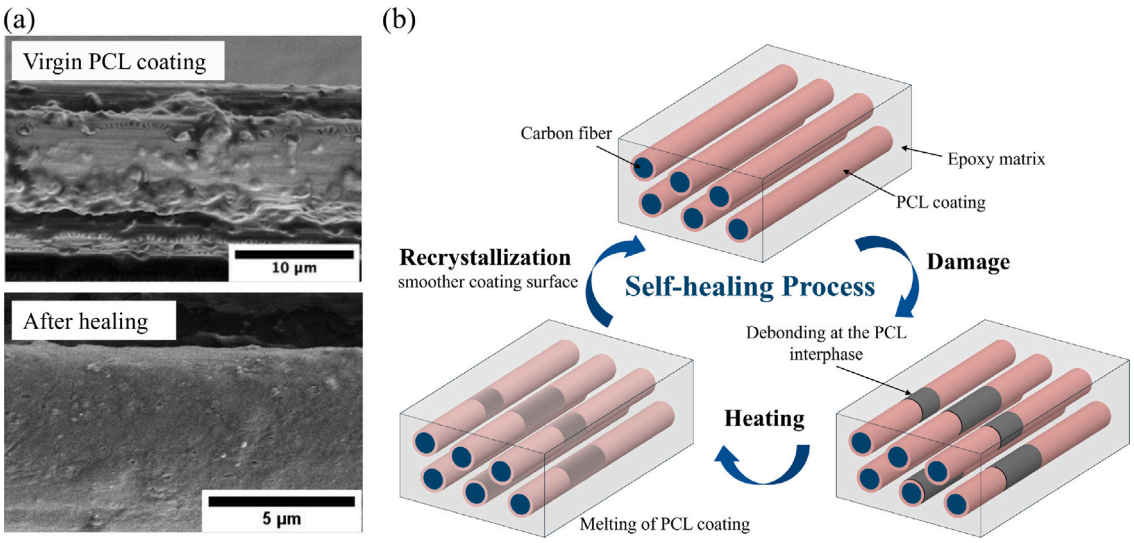

Fig. 1. (a) Field emission scanning electron microscopy images of fiber surface with a self-healing PCL layer: before debonding test and after healing. (Adapted from Simonini et al. [23]). (b) Schematic illustration of the overall mechanism of thermal-activated intrinsic healing process.

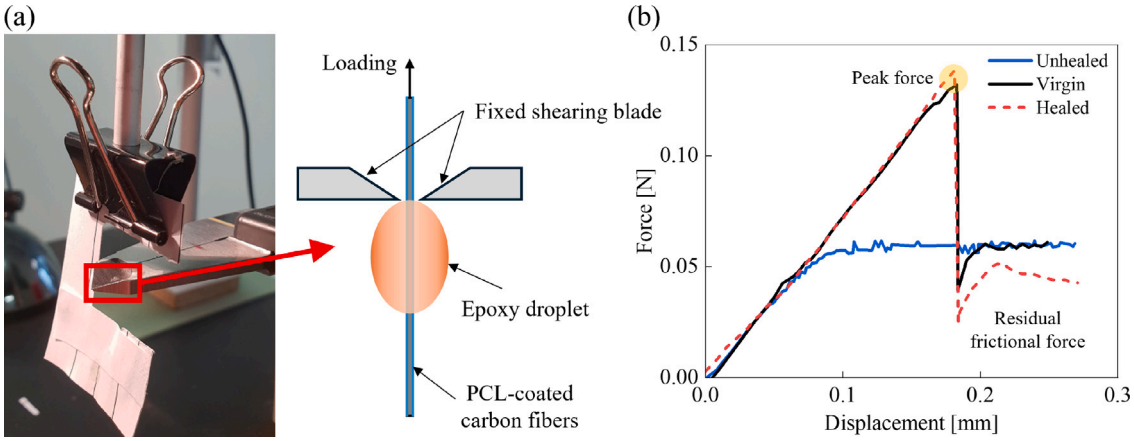

Fig. 2. The microbond test: (a) Schematic of the microbond testing configuration. (b) Force–displacement curve of virgin and healed material. *Source:* Redraw from Simonini et al. [23].

2.3. Field emission scanning electron microscopy

Field emission scanning electron microscopy (FESEM) was used to observe the morphology of CFs with self-healing PCL layers (Fig. 1(a)), as well as the shape of the EP microdroplets. The microscopic images were obtained by using a Zeiss Supra 40 microscope (Zeiss, Germany). All the samples were coated with a platinum/palladium alloy coating (80:20) for 20 s, to make them conductive.

2.4. Microbond test of EP/CF with a self-healing layer

In order to evaluate the self-healing efficiency of the healable interface of epoxy/CF composites, the microbond test was used to assess the interfacial shear strength (IFSS) at the fiber–matrix interface. The microbond test uses two parallel blades to shear the fiber/resin bond by either pushing down on a microdroplet of resin deposited on a single fiber or pulling out the fiber out of a microdroplet (see Fig. 2(a)). A more detailed explanation of the experimental procedure is reported elsewhere by Simonini et al. [23].

The peak force measured during the microbond test is used to calculate the IFSS of the fiber–matrix interface using the equation:

$$\text{IFSS} = \bar{\tau} = \frac{F_{\max}}{\pi d_f L_e} \tag{1}$$

where $\bar{\tau}$ denotes average value of the interfacial shear strength, $F_{\max}$ is the measured peak force, d_f is the fiber diameter and L_e is the fiber embedded length. Subsequently, the healing efficiency H_{eff} can be determined as the ratio of the IFSS of healed ($\bar{\tau}_{\text{healed}}$) and virgin ($\bar{\tau}_{\text{virgin}}$) specimens by:

$$H_{\text{eff}} = \frac{\bar{\tau}_{\text{healed}}}{\bar{\tau}_{\text{virgin}}} \times 100\% \tag{2}$$

Fig. 2(b) shows the representative force–displacement diagrams of the microbond tests for both virgin and healed specimens with a free fiber length of 7.5 mm [23]. Upon the complete interfacial debonding (marked by a sharp peak and subsequent force drop), droplet slippage was observed in the experiments, indicating frictional resistance on the force–displacement curve. Attributed to the smoother PCL layer surface after the healing treatment (as depicted in Fig. 1(a)), the residual frictional force of the healed specimen (≃0.04 N) is reduced compared to that of the virgin specimen (≃0.06 N). The unhealed sample only recovers the frictional force of the virgin sample, without showing any recovery of initial adhesion properties.

3. Finite element model

In this section, a quarter 3D finite element model based on the microbond experiment results by Simonini et al. [23] is established,

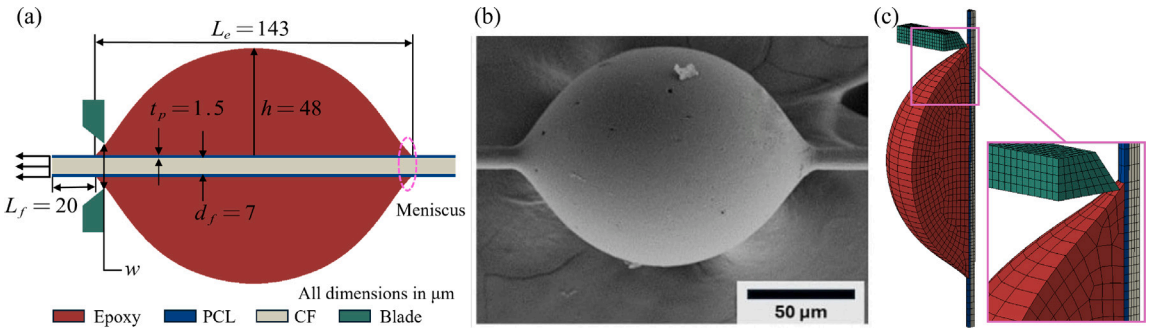

Fig. 3. Finite element model of the microbond test: (a) Materials and dimensions of the finite element model. (b) FESEM image of EP droplet/CF with a PCL layer before testing. (c) A quarter 3D model with finite element meshes.

which is implemented in the commercial software ABAQUS 2023 (Section 3.1). From experimental observations, damage occurs only at the interface between the PCL layer and the epoxy droplet. It is rational to simulate debonding damage as cohesive interface behavior by the definition of surface interaction properties (Section 3.2). In addition, interfacial roughness is investigated in Section 3.3. Thermal stress and surface roughness are considered in both damage and healing models. A fully coupled thermal-stress analysis is performed and takes into account phase change of PCL layer during the healing process (Section 3.4).

3.1. The geometry model

The geometric model is composed of carbon fibers with a PCL layer and an epoxy matrix droplet as presented in Fig. 3(a). The diameter of the carbon fibers d_f is 7 μm. The thickness of the PCL layer t_p is 1.5 μm. The embedded length L_e is 143 μm. The geometry of the droplet is modeled based on the microscopic image (Fig. 3(b)) obtained from the test with the original menisci at two ends of the droplet. Only a quarter of the geometry is modeled to reduce computational cost. The computational model is meshed with element type C3D8R (8-node linear brick, reduced integration with hourglass control) in the damage model and C3D8RT (8-node trilinear displacement and temperature, reduced integration with hourglass control) in the thermomechanical healing model.

The blades are fixed and modeled as a rigid body. From simulation and experiment observations, the mechanical property of the PCL layer is different from pure PCL or bulk PCL. The yield strength of the PCL layer should be much larger than that of pure bulk PCL (approximately 17.28 MPa [40]). Thus, PCL layer is treated as linear elastic in our model to fit the experimental result; otherwise, there should be a plateau after the maximum force rather than brittle damage.

The extended linear Drucker–Prager model is widely used to describe the yield behavior of epoxy resin [31]. The extended linear Drucker–Prager model can be written as:

$$F = t - p\tan\beta - d = 0 \tag{3}$$

where p denote hydrostatic pressure; β represents the slope of the linear yield surface in the p-t stress plane and is commonly referred to as the friction angle of the material; d is the cohesion of the material that can be obtained by $d = \left(\frac{1}{K} + \frac{1}{3}\tan\beta\right)\sigma_t$ (for hardening defined by the uniaxial tension yield stress σ_t), where K is the ratio of the yield stress in triaxial tension to the yield stress in triaxial compression, and thus controls the dependence of the yield surface on the value of the intermediate principal stress. $t = \frac{1}{2}q\left[1 + \frac{1}{K} - \left(1 - \frac{1}{K}\right)\left(\frac{r}{q}\right)^3\right]$, where q is the von Mises stress and r is related to the third invariant of the deviatoric stress tensor. The dilation angle is also required for Drucker–Prager model and this value for thermoset epoxy is close to zero under compression as reported in [41].

Table 1
Material parameters for stress analysis.

Description	Carbon fiber	Epoxy	PCL
Young's modulus (25 °C) [GPa]	312.00[a]	3.10[a]	0.39[a]
Poisson's ratio [–]	0.27[a]	0.31[a]	0.44[a]
Tensile strength [MPa]	3220.00[a]	66.00[a]	17.28 [40]
Friction angle β [°]	–	21.30 [42]	–
Dilation angle [°]	–	0.00 [41]	–

[a] Experimental data measured by Laura Simonini.

Table 1 gives the mechanical properties of each material component. Although the carbon fiber exhibited no damage during the experiment, its tensile strength is provided for reference.

The microbond test was performed by Simonini et al. [23] using a free fiber length of 7.5 mm, whereas a shorter free fiber length of 20 μm is applied in our finite element model to reduce computational cost. As stated by Sockalingam et al. [43], a longer free fiber length only affects displacement. The displacement contribution of the free fiber length can be summed to the numerical data using:

$$U_{cb} = U_o + \frac{FL_f}{E_{\text{eff}}A} \tag{4}$$

where U_{cb} denotes calibrated displacement considering the real free fiber length. U_o is the original calculated displacement using the computational model. F is the load applied on top of the fibers, L_f is the free fiber length, A is the cross-sectional area of the EP/CF composite with a PCL layer, and E_{eff} is the effective elastic modulus of the EP/CF composite with a PCL layer along the longitudinal direction, which can be estimated by the rule of mixture equation $E_{\text{eff}} = E_f V_f + E_c V_c$, E_f and E_c represent elastic modulus of the carbon fiber and the PCL layer, respectively, while V_f and V_c stand for their volume fractions.

Experimental findings indicate that debonding is confined to the epoxy and PCL layer interface, without any visible damage to the epoxy, adhesive failure in the PCL layer, or debonding at the PCL layer and CFs interface. Thus, only debonding at the epoxy/PCL interface is investigated in the computational model. General contact is defined in the whole model, offering a more flexible way to add detail incrementally to the model. By default, general contact uses the finite-sliding formulation, which aligns with the process of the microbond test. Hard contact is used for all the interfaces. Frictionless contact is employed except for the epoxy/PCL interface. The contact property of the epoxy/PCL interface is assigned individually with cohesive behavior and penalty friction. For the cohesive contact modeling approach, cohesive calculations are computed at contact constraint locations, which are primarily associated with secondary nodes. The more refined surface of an interaction typically acts as the secondary surface, which is the surface of PCL layer here. Therefore, the resolution of spatial variations in the cohesive response is usually primarily associated with whichever adjacent body has the more refined surface. The cohesive contact surface model is detailed in the following section.

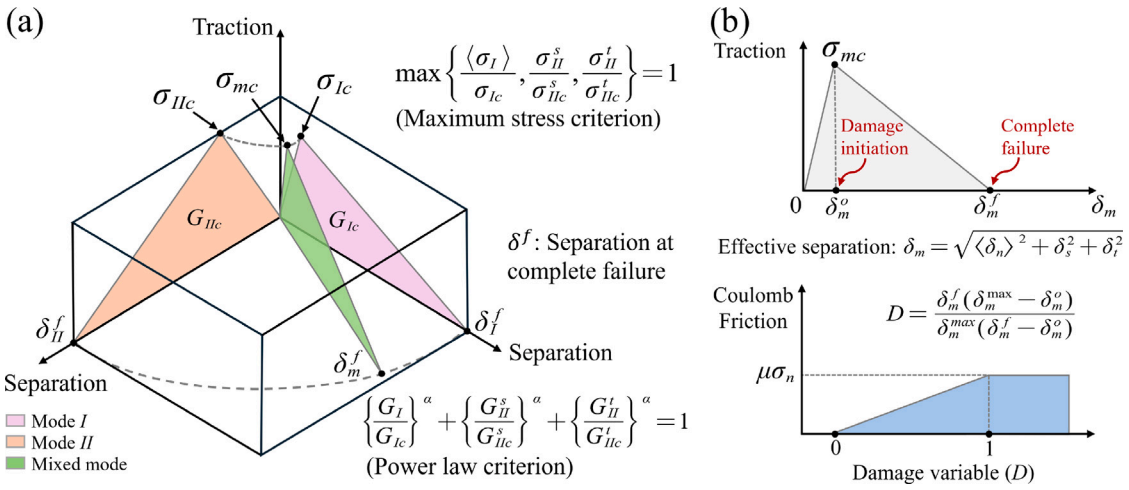

Fig. 4. Cohesive behavior with friction: (a) Bilinear cohesive traction–separation response. (b) Relationship between damage and Coulomb friction.

3.2. Frictional contact interface with cohesive behavior

In order to take both damage and friction into account, the frictional cohesive contact surface property is employed between the epoxy droplet and PCL layer. A bilinear traction–separation law was utilized for cohesive behavior modeling as given in Fig. 4(a). The current interface model utilizes a maximum stress criterion for the onset of damage and a mixed-mode power law criterion for the evolution of damage as follows:

$$\max\left\{\frac{\langle\sigma_I\rangle}{\sigma_{Ic}}, \frac{\sigma^s_{II}}{\sigma^s_{IIc}}, \frac{\sigma^t_{II}}{\sigma^t_{IIc}}\right\}=1 \tag{5}$$

$$\left\{\frac{G_I}{G_{Ic}}\right\}^\alpha+\left\{\frac{G^s_{II}}{G^s_{IIc}}\right\}^\alpha+\left\{\frac{G^t_{II}}{G^t_{IIc}}\right\}^\alpha=1 \tag{6}$$

where $\langle\cdot\rangle$ is the Macaulay bracket, which equals σ_I if $\sigma_I > 0$, otherwise zero. σ is traction and σ_c is strength. The sub-indices I and II refer to the fracture modes mode I and mode II, respectively. Interfacial damage evolution is given a critical energy release rate, G_c, to define complete debonding at the interface. A linear interaction law was employed to capture crack-tip mode mix during crack growth, i.e., $\alpha = 1$. For both the first and second shear directions (denoted as s and t, respectively), the mode II critical energy release rate G_{IIc} is set to 190 J/m^2 and the interfacial strength value is 48 MPa to fit the experimental results. Properties for modes I are assumed to be equal to the mode II because mode II is the predominant failure mode and changing properties of modes I has little effect on the force–displacement curve, as reported in Ref. [43].

As mentioned in Section 2.1, carbon fibers coated with PCL initially have a rough texture, which becomes smoother after the thermally activated healing process. A rough surface that has a stochastic shape is difficult to model exactly. The main parameter that describes the surface as a mechanical component is the coefficient of friction [44]. In ABAQUS, it is feasible to define frictional tangential behavior for cohesive contact surfaces [45]. As demonstrated in Fig. 4(b), when cohesive bonding at a specific interface location is intact, tangential motion resistance relies solely on cohesive behavior. As cohesive damage begins to accumulate at a certain interface location ($\delta \geq \delta^0$), the shear stress at the interface is influenced by both the cohesive and friction models, with the friction model contribution being weighted by the scalar damage variable (D) of the cohesive behavior. Once the cohesive bond is completely damaged ($\delta \geq \delta^f$), the shear stress at the interface is determined only by the friction model. In the computational model, tangential behavior with Coulomb friction is assigned to the virgin and healed interfaces. The frictional stress is determined by multiplying the interface compressive normal stress σ_n with the coefficient of friction μ.

3.3. Surface roughness induced frictional stress

Existing computational models for microbond tests typically focus on the residual stress and relate it to frictional force through Coulomb friction; however, our simulation addresses that residual stress is not the only contribution to frictional forces. From available research, the frictional resistance to sliding will depend upon both residual stresses and the surface roughness [46,47]. Interfacial debonding and sliding processes between two rough surfaces are generally complicated processes [48]. As illustrated in Fig. 5, the virgin EP/CF with a PCL layer before testing exhibit a notably rough and irregular surface as a consequence of the presence of the PCL layer. When two rough surfaces slide against each other, the interaction is dominated by the contact between microscopic surface irregularities known as asperities. During sliding, the interlocking and subsequent deformation of asperities lead to further localized compression at the contact junctions [49], which plays a crucial role in the frictional behavior of the surfaces.

To account for surface roughness effects, we introduce an additional frictional shear stress at the interface of epoxy and PCL, inspired by Marshall et al. [50]. They conducted single-fiber pull-out tests and concluded that a micromechanical model with constant frictional shear stress better aligned with experimental data than a Coulomb friction-based model. In our model, the frictional shear stress during partial sliding (initial debonding) is assumed to increase linearly with the interfacial debond length to fit the experimental data, which is given by:

$$\sigma_f = \frac{L_d}{L_e}\sigma_f^{max} \tag{7}$$

where σ_f and σ_f^{max} represent the present frictional shear stress and the maximum applied frictional shear stress, respectively. L_d denotes the present debond length, while L_e is the embedded length of the epoxy droplet, or the maximum debond length. During the sliding phase, the frictional shear stress remains constant after complete debonding. The required frictional shear stress σ_f^{max} can be obtained by:

$$\sigma_f^{max} = \frac{F_f - F_f^T}{\pi D L_e} \tag{8}$$

where F_f represents total frictional force and F_f^T is the frictional force induced by thermal residual compressive stress only. D is the diameter of the PCL-coated fibers. L_e denotes the embedded fiber length.

3.4. Thermomechanical healing model

In preparing virgin microdroplet samples, a curing temperature of 50 °C is used, which is lower than the melting point (T_m) of PCL (60 °C).

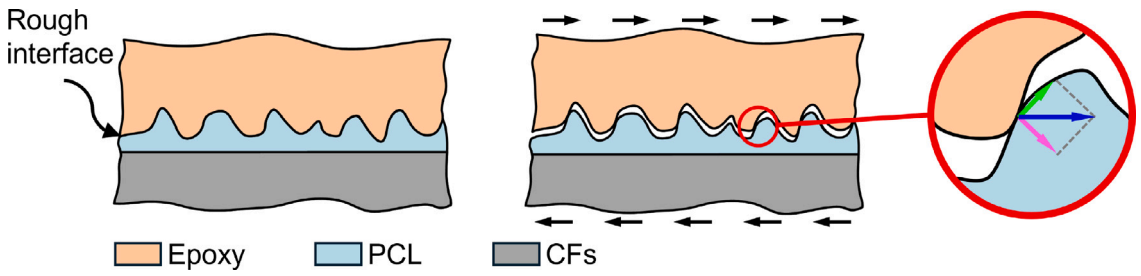

Fig. 5. Schematic illustration of the contact pressure induced by surface roughness/asperities.

Thermal stress can be easily derived from a predefined temperature field and the coefficient of thermal expansion (CTE). However, the temperature of the healing process is higher than the melting point of PCL; PCL melts and recrystallizes to heal the debonded interface. Thus, in the thermal analysis of healed material, it is important to account for the temperature-dependent elastic modulus of PCL and the heat generation associated with its phase change.

During the healing process, an electric current was applied on CFs for a duration of 15 s and the surface temperature of CFs rises from room temperature (25 °C) to 75 °C due to the Joule heating effects [23]. Subsequently, the sample was allowed to cool down to ambient room temperature due to thermal radiation. A fully coupled thermal-stress analysis with transient response is performed to solve simultaneously for the stress/displacement and the temperature fields. Surface thermal radiation is present in both heating and the cooling phases. The net rate of radiation heat transfer from the sample surface to the surrounding q''_{rad} can be achieved by the Stefan–Boltzmann law [51]:

$$q''_{\text{rad}} = \varepsilon_{em}\sigma(T_s^4 - T_{\text{sur}}^4) \tag{9}$$

where ε_{em} denotes emissivity. σ is the Stefan–Boltzmann constant, $\sigma = 5.67 \times 10^{-8}$ W/(m^2 K^4). T_s and T_{sur} represent ambient temperature and surface temperature, respectively.

In the thermomechanical healing model, the debonded interface is initially assumed to be perfectly repaired due to the rapid healing observed in the experiment. Thermal contact resistance is neglected in the computational model. Despite the roughness of the epoxy/PCL interface, the true contact area approaches the nominal area due to PCL flow, reducing the interfacial thermal contact resistance to a negligible level compared to the rest of the conduction path.

As temperature rises, the Young's modulus of PCL is assumed to decrease linearly until reaching the melting point, where it remains constant. The PCL layer is assumed to melt completely upon reaching its melting point. Due to the phase change of PCL from liquid to solid state, it is necessary to account for exothermic reaction heat during the recrystallization process. The general governing equation for the three-dimensional transient heat transfer problem is:

$$\rho C_p \frac{\partial T}{\partial t} = k_x\left(\frac{\partial^2 T}{\partial x^2}\right) + k_y\left(\frac{\partial^2 T}{\partial y^2}\right) + k_z\left(\frac{\partial^2 T}{\partial z^2}\right) + Q \tag{10}$$

where ρ is density, C_p is specific heat, k_x and k_y are coefficients of thermal conductivity in the $x-$ and $y-$ directions, respectively. The volumetric heat source term (Q) represents the internal volumetric heat generation taking place during the phase change of PCL. In this model, it is relevant to rate of crystallinity of PCL and can be expressed as:

$$Q = \rho \Delta H_f \frac{dX_c}{dt} \tag{11}$$

where ρ is the density of PCL, ΔH_f corresponds to overall enthalpy of 100% crystalline PCL. X_c is the relative crystallinity of PCL and can be obtained by [52]:

$$X_c = \frac{\int_{t_0}^{t}(dH/dt)dt}{\int_{t_0}^{\infty}(dH/dt)dt} \tag{12}$$

Table 2
Material parameters for thermal analysis.

Description	Carbon fiber	Epoxy	PCL
Density [g/cm^3]	1.71[a]	1.20[a]	1.10[a]
CTE [ppm/°C]	12.00 [57]	60.00[b]	134.00[b]
Thermal conductivity [W/m K]	21.00 [58]	0.20 [59]	0.46 [60]
Specific heat [J/kg K]	984.00 [61]	1400.00 [60]	2000.00 [62]
ΔH_f [J/g]	–	–	163.00 [63]
Emissivity [–]	0.78 [58]	0.96 [64]	–
Avrami index [–]	–	–	1.93 [63]
Crystallization rate constant [min^{-n}]	–	–	2.27 [63]
Melting point [°C]	–	–	60.00[b]
Glass transition temperature [°C]	–	80.00[b]	–

[a] Manufacturer datasheet.
[b] Experimental data measured by Laura Simonini.

where, t_0 is the onset temperature of crystallization and dH/dt the heat flow rate.

The Avrami equation [53–55] has been widely used to characterize the isothermal crystallization kinetics of many polymer systems. The crystallization process of PCL could be described by the Avrami equation as follows:

$$1 - X_c = \exp[-Kt^n] \tag{13}$$

where, X_c is the relative crystallinity, K is the crystallization rate constant in the isothermal crystallization process, and the parameter n is the Avrami exponent, which determines the crystal geometry and nucleation type. By taking natural logarithms, Eq. (13) can be organized into the following form:

$$\ln[-\ln(1 - X_c)] = \ln K - n \ln t \tag{14}$$

According to Nie et al. [56], there is a linear relationship between $\ln[-\ln(1 - X_c)]$ and $\ln t$ for pure PCL. By linear fitting, the values of n and K can be calculated from the slope and intercept of the linear plot of $\ln[-\ln(1 - X_c)]$ versus $\ln t$. Heat generation defined in Eq. (11) is implemented in the thermomechanical model through the use of HETVAL subroutine in ABAQUS.

Table 2 gives the material properties used in the thermomechanical model.

Finally, it should be noted that finite element models that incorporate contact and cohesive surfaces often experience convergence difficulties and can be time-consuming. For a correct and efficient run of the finite element solver, some advice is given as follows:

(a) Nonlinear effects should be included in the analysis step of ABAQUS when using the cohesive contact with large sliding displacements, and automatic stabilization can be chosen to stabilize unstable static problems.
(b) For some increments, customized general solution control is needed to adjust the convergence algorithms. By default, maximum number of cutbacks allowed for an increment I_A is 5, but this might require an increased value to 10.

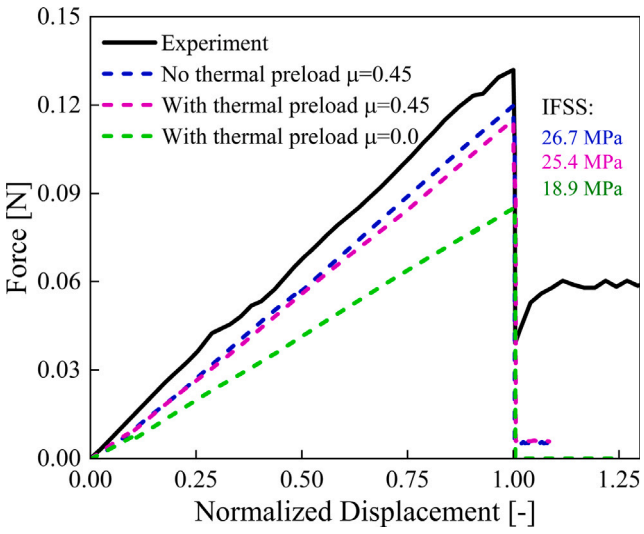

Fig. 6. Effects of thermal preload and friction on simulated force-normalized displacement curves of the microbond test for virgin material.

(c) The contact stiffness parameter should be adjusted thus to result in an acceptably small penetration of the surfaces and a reliable convergence of the iterative solution. Convergence issues related to highly stiff contact behavior can be reduced by lowering contact stiffness.

4. Results and discussion

In this section, the FE analysis is firstly conducted to explore the effects of thermal stress and surface roughness on the interfacial performance of the virgin EP/CF with a PCL layer and to determine the model parameters validated by the microbond test. Then, the mechanical performance of the healed material is evaluated considering the phase change of PCL during the healing process.

4.1. Mechanical performance of virgin EP/CF with a PCL layer

4.1.1. Thermal residual stress and Coulomb friction

In the microbond test [23], epoxy droplets were deposited onto single fiber filaments of CFs and cured at a maximum temperature of 50 °C, which is below the T_m of PCL to preserve the original morphology of the PCL nanoparticles as much as possible. Noted that although the T_m of PCL is approximately 60 °C, partial melting can occur at lower temperatures, such as 50 °C [65]. Thermal residual stresses arising from thermal shrinkage as the material cools from curing temperature (50 °C) to room temperature (25 °C) are simulated by introducing a predefined temperature field into the computational model. The maximum curing temperature is commonly defined as the stress-free temperature when calculating residual stress [43,66]. A thermal preload of −25 °C is applied according to experimental conditions. Due to thermal expansion mismatch among the carbon fibers, the PCL layer, and the epoxy droplet, the thermal residual stress may lead to residual compressive radial forces around the fiber and results in non-zero sliding force after complete debonding.

The force-normalized displacement curves predicted by the simulation with and without thermal preload and friction are shown in Fig. 6. Calculated IFSS is also given according to Eq. (1). In this case, only Coulomb friction related to thermal shrinkage is considered. The solid line depicts the force-normalized displacement curve in the microbond test for comparison. The model with a friction coefficient of 0.45 and no thermal preload exhibits the highest peak load and interfacial strength, while the model with thermal preload and no friction displays the lowest peak load and interfacial strength. The peak force for the model with both thermal preload and Coulomb friction lies in between. It can be observed that the peak force and interfacial strength increase with a higher coefficient of friction but decrease in the presence of thermal stress.

From the numerical results, the frictional force predicted by Coulomb friction (≃0.006 N) shows significant discrepancy with the data measured in the experiment, where remains a frictional force of about 0.06 N after debonding at the interface of epoxy and PCL. It can be explained that the curing temperature (50 °C) in the microbond test is kept below the melting point of PCL material, which is comparable to the room temperature (25 °C), leading to a low thermal preload (−25 °C). Moreover, CTE of PCL layer is higher than that of epoxy, which reduces the compressive stress due to thermal contraction at the interface. Specifically, as shown in Fig. 7, thermal preload and Coulomb friction are both accounted for in the result presented. Although the maximum Mises stress in the virgin sample can reach 84.7 MPa when the epoxy is completely cured and cooled to ambient room temperature, the contact pressure at the interface is only 4.2 MPa.

As a result, there should be additional compressive stress, apart from simple Coulomb friction related to thermal contraction, that contributes to the frictional force observed in the experiment. As discussed in Section 3.3, surface roughness significantly contributes to compressive stress, which will be explored in the following section.

4.1.2. Influence of surface roughness

In order to account for surface roughness, a debond-length-dependent frictional shear stress as given in Eq. (7) is applied at the EP/PCL interface. According to Eq. (8), a maximum frictional stress of 12 MPa can be achieved from experimental data. The force-normalized displacement curve of the virgin material predicted by the calibrated model considering surface roughness is demonstrated in Fig. 8(a). It can be seen that the numerical result obtained is consistent with the experimental curve for both the peak force and the frictional force after debonding. The simulated peak force increases due to the surface-roughness-induced frictional stress, resulting in higher interfacial strength. Thus, roughness asperities can enhance the frictional shear stress at the interface and impart significant toughness. It should be noted that during sample preparation, EP cross-linking is incomplete at 50 °C, leading to further cross-linking during the healing process. This additional cross-linking can cause shrinkage and introduce residual stress in the healed materials. In our computational model, the cure kinetics of EP were not considered; therefore, the fitted frictional shear stress of 12 MPa is not solely induced by surface roughness but also includes contributions from EP shrinkage.

Fig. 8(b) illustrates the progressive interfacial debonding, where 1.0 represents complete damage and 0.0 represents an intact state. Debonding initiates at the menisci, spreading from the blade contact side. Subsequently, the damage extends to other sides and propagates along the interface until complete debonding is achieved.

Fig. 9 demonstrates the simulated and the tested epoxy droplets after complete debonding, respectively. As seen in Fig. 9(a), the epoxy droplet exhibits residual deformation where the blades are positioned after unloading, which is consistent with the experimental findings in Fig. 9. The gap width between blades, as measured in Fig. 9(b), is 13 μm and is employed in the computational model for the virgin material. Experimental results also indicate that the menisci at both ends are no longer present after the microbond test.

4.2. Mechanical performance of healed EP/CF with a PCL layer

4.2.1. Healing process and thermal residual stress

In order to heal the debonded interface, the specimen was heated by applying a voltage of 5.0 V on carbon fibers for 15 s. The applied voltage was an optimal value balancing desired healing temperature

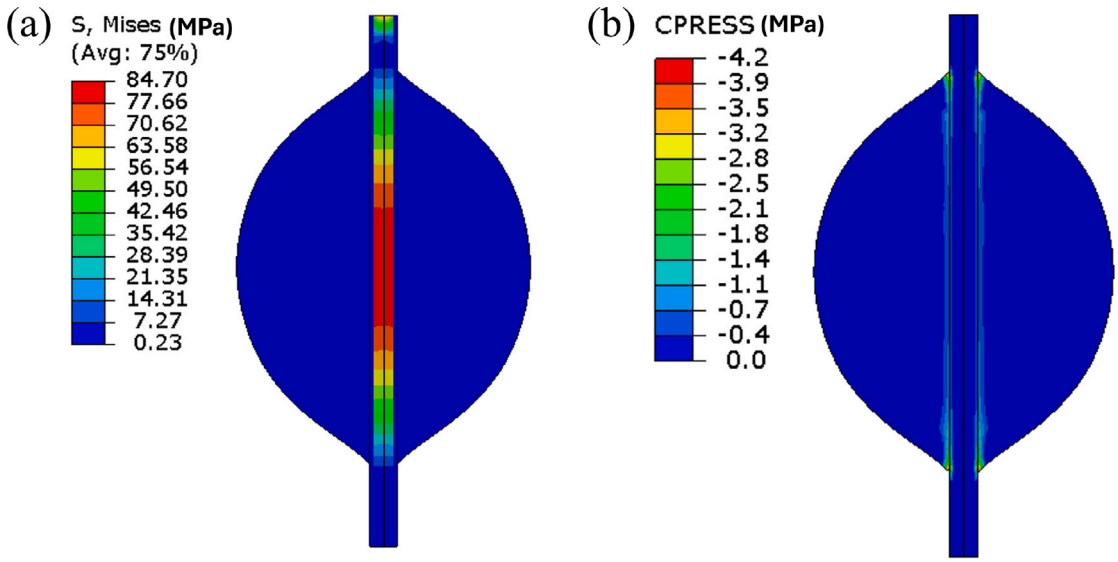

Fig. 7. Thermal stress in virgin specimen after curing of epoxy droplet (with thermal preload, μ = 0.45): (a) Distribution of von Mises stress; (b) Distribution of contact stress.

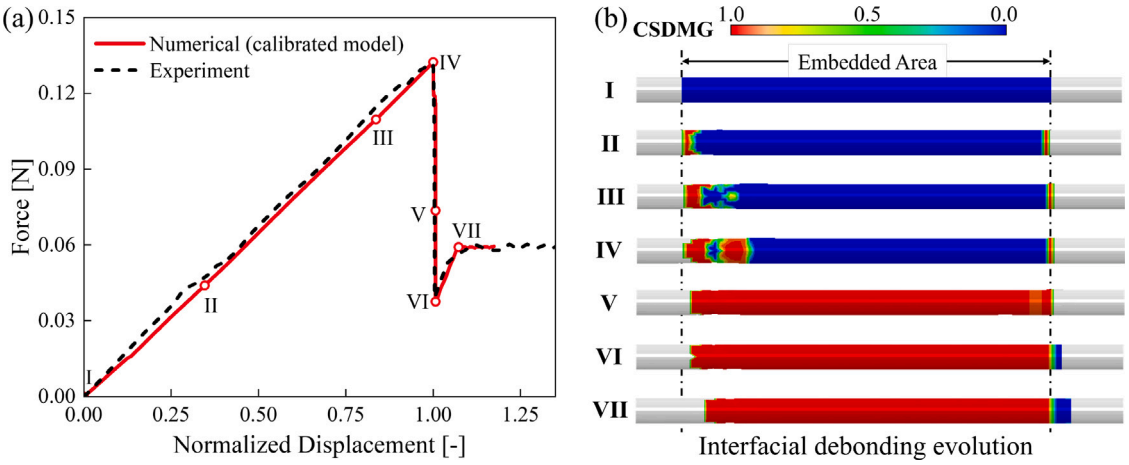

Fig. 8. Calibrated model considering surface roughness: (a) Simulated force-normalized displacement curve comparing with experimental data; (b) Scalar stiffness degradation for cohesive surfaces (CSDMG) at different phases (1.0 represents complete debond and 0.0 denotes intact interface).

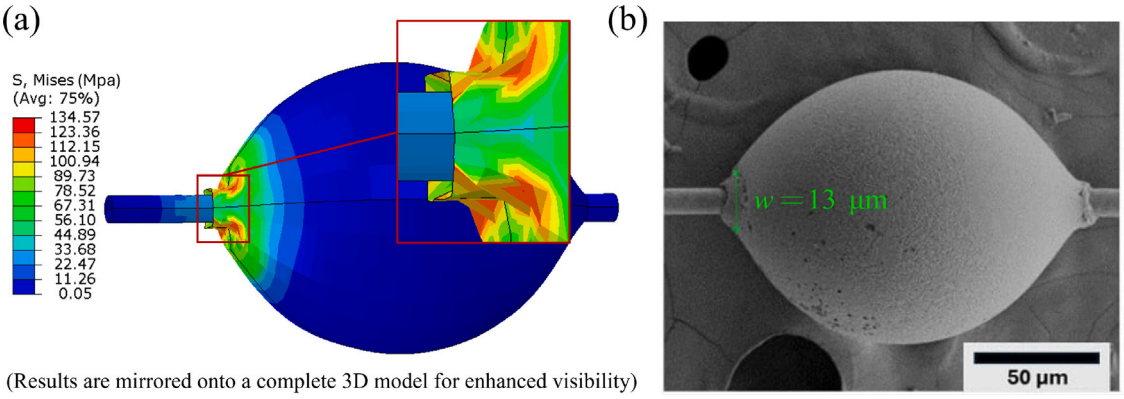

Fig. 9. Epoxy droplet after complete debonding: (a) Mises stress of the deformed epoxy droplet model after complete debonding (CF is hidden for visualization of stress distribution on epoxy droplet). (b) FESEM image of fully debonded epoxy droplet.

and structural integrity of the fiber [23]. The glass transition temperature (T_g) of the EP was measured to be 80 °C. To achieve optimal healing efficiency, the healing temperature should be set close to the T_g as reported in [21]. Due to the Joule effect, the surface temperature

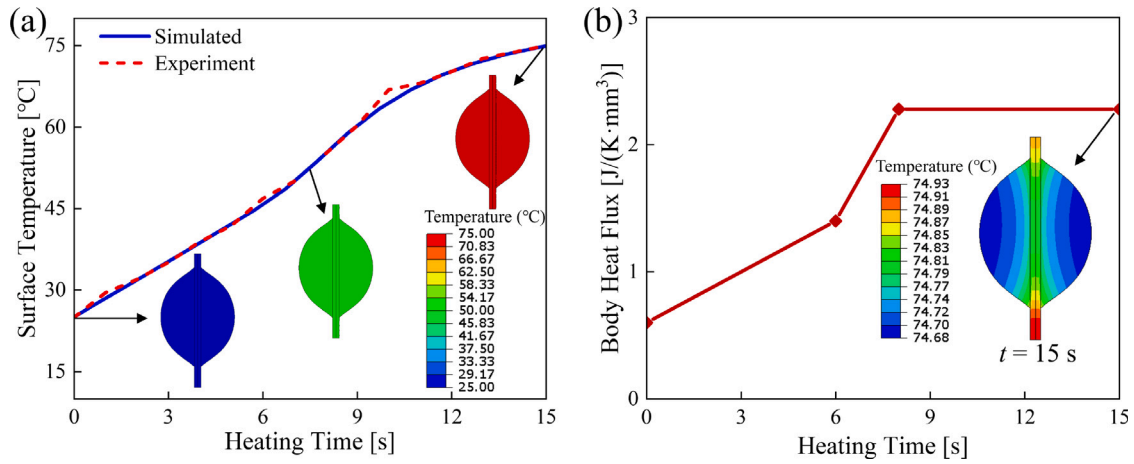

Fig. 10. Heating process: (a) Temporal surface temperature of a single carbon fiber during Joule heating (Experimental result was redraw from Simonini et al. [23]). (b) Equivalent body heat flux applied in carbon fibers.

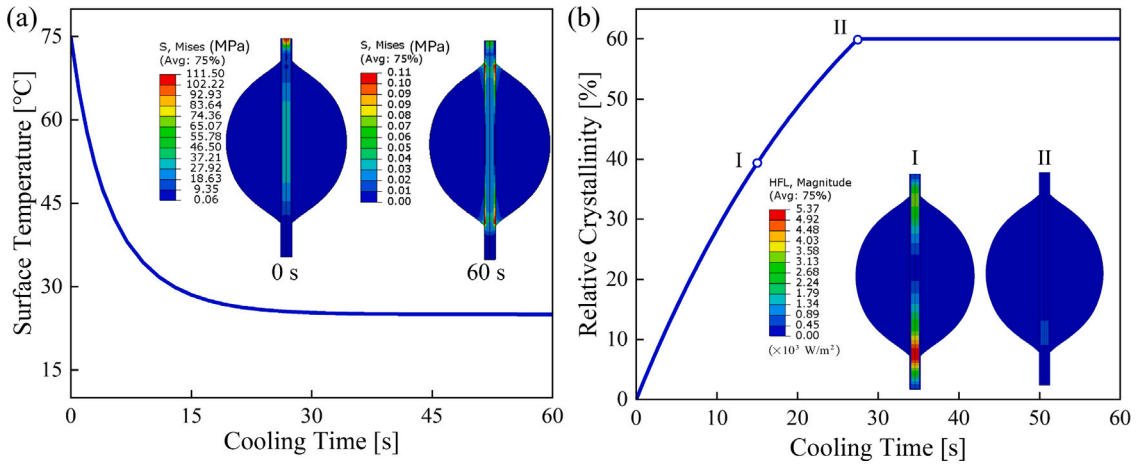

Fig. 11. Computational modeling of cooling process: (a) Calculated temporal surface temperature and thermal stress distribution of the specimen. (b) Calculated crystallinity of PCL versus cooling time and heat flux distribution in the specimen.

of a single carbon fiber elevated from room temperature (25 °C) to 75 °C. During heating, the PCL layer melted and healed the debonding upon recrystallization. In our model, the carbon fiber is equivalent to a volumetric heat source, with Joule heat generation equivalent to a body heat flux, which is fitted to the experimental result.

Fig. 10(a) shows the simulated and the tested results, and Fig. 10(b) gives the equivalent body heat flux applied in carbon fibers. As given in Fig. 10(a), it can be seen that the simulated temperature history on the fiber surface fits the tested results well. Thus, through this equivalent method, thermal gradients and mechanical deformation can be captured simultaneously without modeling electrical conduction explicitly. Furthermore, the simulation results presented in Fig. 10(a) reveal a relatively uniform temperature distribution across the specimen throughout the entire heating process, which is more evident in the thermal map depicted in Fig. 10(b) with a more detailed color gradient range. This phenomenon can be largely attributed to the specimen's microscopic scale. In specimens on the order of microns, the distances over which heat must travel are minimal, facilitating rapid thermal equilibration across the entire material. This efficient heat conduction minimizes the development of significant thermal gradients, as any localized temperature variations are quickly dissipated. Consequently, instead of solving the full heat diffusion equation using heat flux, the simulation can also be simplified by directly applying a uniform time-dependent temperature condition across the entire domain.

Following Joule heating, the specimen can be cooled rapidly to room temperature (25 °C) due to thermal radiation. Heat generation due to recrystallization of PCL can be achieved by Eq. (11) and implemented using HETVAL subroutine. The parameters used for the recrystallization simulation were obtained from the existing literature, as detailed in Table 2.

Fig. 11(a) demonstrates the surface temperature decreasing with time during cooling and the von Mises stress distributions for the specimen before (0 s) and after (60 s) cooling. The specimen is rapidly cooled to room temperature in approximately 30 s and stabilizes thereafter. Upon completion of heating (before cooling), the maximum thermal stress is about 111.50 MPa, which significantly decreases to 0.11 MPa after cooling for 60 s. As a result, the thermal preload in the healed specimen is negligible due to the low thermal stress achieved.

Fig. 11(b) shows the evolution of relative crystallinity of PCL and heat flux distribution in the cooling process. PCL is a semicrystalline polyester whose degree of crystallinity at room temperature can vary significantly with processing conditions, molecular weight, and thermal history. In many reports, neat PCL is found to have a crystallinity in the range of about 30%–60% at room temperature. Coburn et al. [67] reported a bulk-PCL crystallinity of 60%, which is utilized in our simulation. It is observed that the relative crystallinity of PCL increases with prolonged cooling times, eventually reaching a maximum of 60% at the turning point of the cooling curve (29.26 s). As shown in Fig. 11(a), this also marks the time point when the specimen approaches ambient temperature. And at this moment, the heat flux within the specimen approaches zero, as indicated by the heat flux contours.

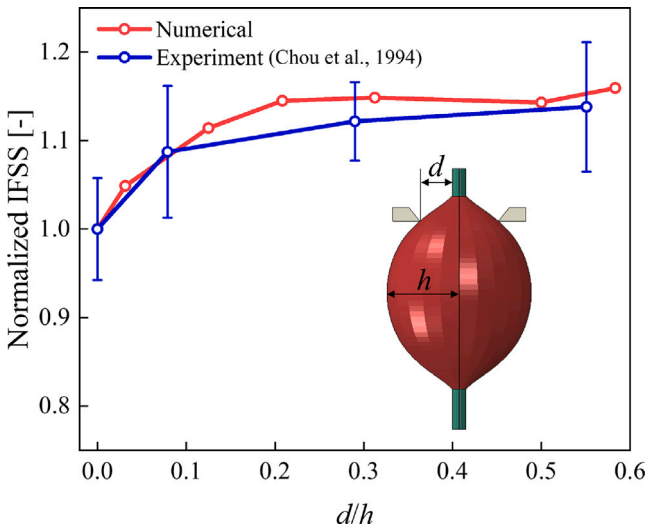

Fig. 12. Effect of fiber-to-blade distance on average interfacial shear strength.

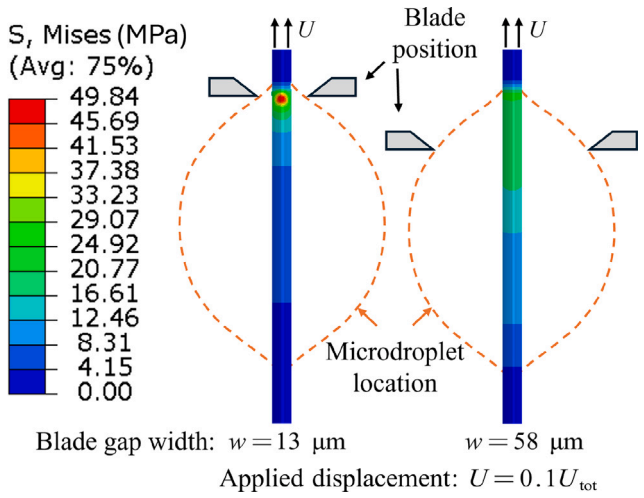

Fig. 13. Stress distribution at epoxy/PCL Interface for different blade positions at $U = 0.1U_{tot}$.

In a nutshell, the healing process by heating and cooling the specimen can not only repair the interface but also reduce the thermal residual stress. Indeed, heat treatment is one of the most widely used stress relief methods by heating, holding, and cooling the material for a specific time [68]. Within the context of the simulated conditions, the thermal residual stress in the healed specimen after healing treatment is very low and negligible. Additionally, the required cooling time can be estimated from the recrystallization time of PCL.

4.2.2. Influence of blade position on microbond test result

In the microbond test, the positions of shearing blades significantly influence the mechanical response. Fig. 12 demonstrates the normalized IFSS for FE models with different fiber-to-blade distances (d) and compares it with the experimental results based on Kevlar 49/Epon 828 specimens by Chou et al. [69]. The normalized IFSS is the ratio of IFSS for any blade position to IFSS for zero distance between fiber and blade. The size effect is reduced by using d/h, where h is the radius of the droplet. Seven ratios ranging from 0 to 0.58 are considered in the simulation. Despite the use of different materials in our study compared to the experiment by Chou et al. [69], both numerical and experimental findings indicate an increase in average IFSS values with larger fiber-to-blade distance or gap width between blades. A similar finding was reported by Zhi et al. [70] who evaluated how various fiber-to-blade distances influence the IFSS between polyester fibers and epoxy resin.

In order to explain this experimental observation, Miller et al. [71] postulated that applying load close to the fiber results in concentrated shear stress at the top of the droplet, while the lower portion experiences small interfacial shear stress. Conversely, applying the load further from the fiber causes the maximum stress point to shift downwards, reducing the stress magnitude. Consequently, if the interface fails when stress surpasses a critical level, a droplet loaded closer to the fiber would debond under less force compared to one loaded further away, due to higher stress concentration, which would also lead to a lower calculated IFSS.

Here, we validate the postulation of Miller et al. [71] in our FE simulation. Fig. 13 depicts the von Mises stress distribution at the EP/PCL interface when the applied displacement on the top of the fiber is one-tenth of the total displacement. Numerical models with two different blade gap widths (13 μm and 58 μm) measured from SEM micrographs are analyzed. It can be observed that stress concentration noticeably decreases with increasing blade gap width, and the model with a 58 μm gap exhibits lower maximum stress compared to the 13 μm gap model. Therefore, it is necessary to position the blades at a constant fiber-to-blade distance due to its influence on shear stress distributions along the interface.

4.3. Healing efficiency

As mentioned earlier, the gap width between blades is determined from the SEM micrographs of debonded epoxy microdroplets. The blade gap width for the virgin material is 13 μm as indicated in Fig. 9(b) and 58 μm for healed material as given in Fig. 14(a). Fig. 14(b) demonstrates the simulated and experimental force-normalized displacement curves for the healed material. The simulated curves correspond well with the experimental results. The computational model with a blade gap width matching the SEM micrograph of the healed material exhibits a better fit compared to the model with a smaller blade gap width.

According to Eq. (2), the healing efficiency of the healed material can be obtained by the ratio of the IFSS of healed and virgin specimens. The results are demonstrated in Fig. 15. The experimental healing efficiency is $107.3 \pm 10\%$, and it is 99% for model with blade gap width of 13 μm and 107.6% for the blade gap width of 58 μm. A wider blade gap width could result in an overestimation of healing efficiency. Thus, maintaining a constant gap of blades is necessary to minimize experimental variability. The concept of employing a pin-holed steel film, as suggested by Choi et al. [72], could potentially achieve this objective. It should be noted that the blade gap width is not the sole factor contributing to the higher measured IFSS. Additionally, the potential nucleation effect of the fiber may enhance the crystallization ability of PCL, thereby improving healing efficiency. In our computational model, the droplet size is kept constant; however, in the experimental setup, it varies across different samples. Furthermore, the sample geometry also influences the measured IFSS [73], which deserves further investigation in future work.

5. Conclusions

In this study, a 3D thermomechanical model with a frictional cohesive surface is developed to explore the damage and healing characteristics of the novel EP/CF composite with a nanostructured PCL layer. The effect of surface roughness is firstly addressed in the computational model for the microbond test by incorporating a debond-length-dependent frictional shear stress. The proposed computational model is effectively validated by microbond tests.

For the virgin material, Coulomb friction and thermal stress induced by epoxy curing are firstly analyzed. The numerical results indicate that the IFSS increases with a higher coefficient of friction and decreases in the presence of thermal stress. Moreover, surface roughness is considered in our model and the simulation reveals that roughness asperities

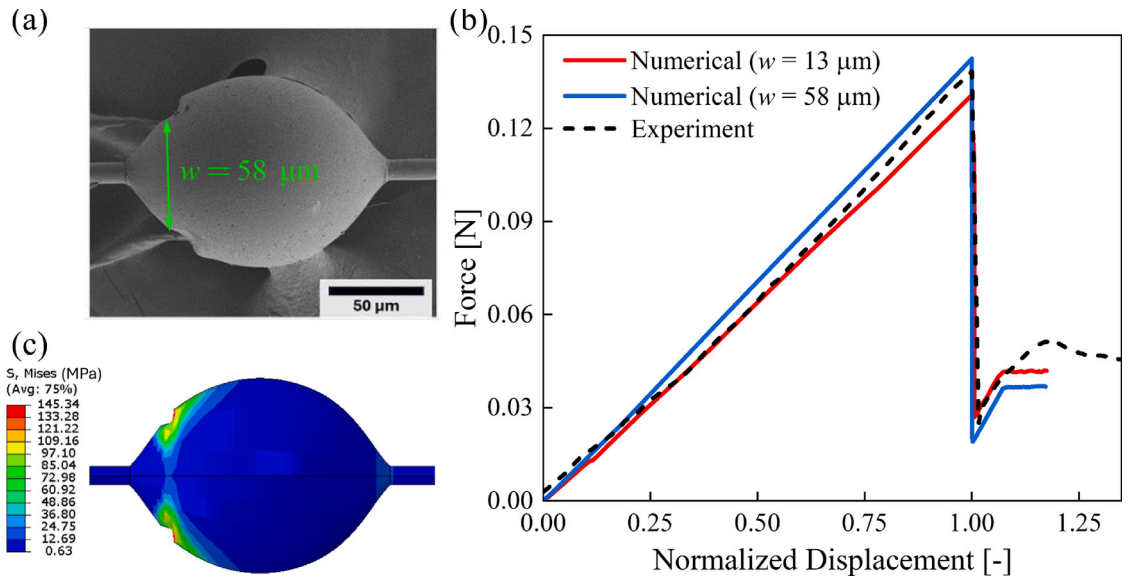

Fig. 14. (a) FESEM image of debonding healed EP droplet; (b) Simulated von Mises stress distribution of debonding healed EP droplet; (c) Force-normalized displacement curve of healed model.

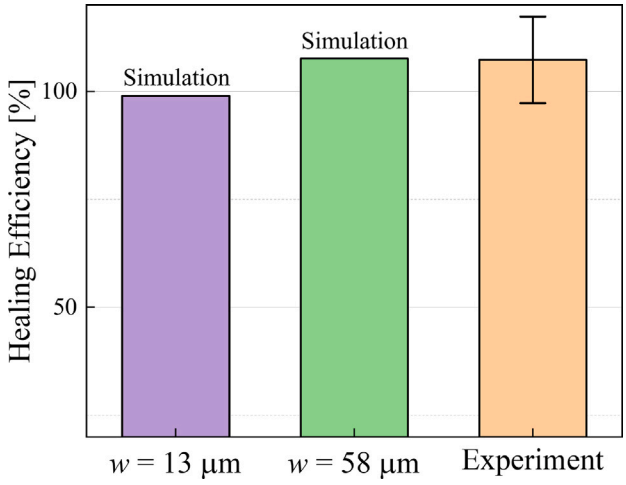

Fig. 15. Healing efficiency of EP/CF with a repairable interface.

can enhance the frictional shear stress at the interface and impart significant toughness. It is also observed that interfacial debonding initiates at the menisci from the blade contact side.

For the healed material, a fully coupled thermal-stress procedure is developed. An equivalent body heat flux is employed to simulate the Joule heating in the carbon fiber. A relatively uniform thermal map across the specimen throughout the entire heating process indicates that the simulation can be simplified by directly applying a uniform predefined temperature field across the entire domain instead of solving the full heat diffusion equation using heat flux. Furthermore, to account for the phase change of the PCL layer in heating and cooling, a temperature-dependent modulus is utilized for PCL. Besides, heat generation during recrystallization of PCL is considered using `HETVAL` subroutine. It is found that the healing process can not only repair the interface but also reduce the thermal residual stress. The thermal residual stress in the healed specimen after healing treatment is very low and negligible, and the recrystallization time of PCL can be calculated to estimate the required cooling time of the specimen. In addition, the influence of blade gap width on calculated average IFSS is investigated. The findings show that the IFSS values rise as the blade gap width increases and blade positions significantly affect the shear stress distribution along the interface. Thus, it is necessary to maintain a constant fiber-to-blade distance to minimize experimental variability.

Despite the contributions of this study, several limitations should be acknowledged. First, in calculating residual stress, only thermal shrinkage is considered, while the effects of epoxy cure kinetics and associated chemical shrinkage are neglected. Second, the potential nucleation effect of the fiber, which may enhance the crystallization ability of PCL and thereby improve healing efficiency, is not explicitly modeled. Third, the influence of sample size on the measured IFSS is not taken into account. Despite these limitations, this study provides some valuable insights into improving the durability of composite structures by incorporating self-healing interfaces. Future research could address these limitations by integrating cure kinetics into the computational model, more diverse samples and simulations through improved experimental techniques.

CRediT authorship contribution statement

Yulin Sun: Writing – original draft, Visualization, Validation, Methodology, Investigation, Formal analysis, Data curation, Conceptualization. **Laura Simonini:** Writing – review & editing, Validation, Resources, Investigation, Data curation. **Chen Xing:** Writing – review & editing, Methodology, Formal analysis. **Leon Mishnaevsky:** Writing – review & editing, Writing – original draft, Supervision, Project administration, Methodology, Funding acquisition, Conceptualization.

Declaration of competing interest

The authors declare that they have no known competing financial interests or personal relationships that could have appeared to influence the work reported in this paper.

Acknowledgments

The authors acknowledge the financial support of the European Commission via Horizon project “Blades2Build: Recycle, repurpose and reuse end-of-life wind blades composites: A coupled pre- and co-processing demonstration plant”, grant agreement 101096437, and of the Ministry of Foreign Affairs of Denmark via Danida grant 19-M02-DTU “Maintenance and repair strategy for wind energy development”

(maintainergy.dk). LM is grateful to the Velux Foundation, Denmark for its support of the project PREMISE "Preventing MIcroplastics pollution in SEa water from offshore wind". We thank Prof. Bent Fruergaard Sørensen (DTU Wind) for useful discussions on numerical modeling.

Data availability

Data will be made available on request.

References

[1] F. Libonati, L. Vergani, Damage assessment of composite materials by means of thermographic analyses, Compos. Part B: Eng. 50 (2013) 82–90, http://dx.doi.org/10.1016/j.compositesb.2013.01.012.

[2] X. Li, C. Zhou, C. Xing, A. He, J. Yu, G. Wang, A phase-field fracture model for fatigue behavior in fiber-reinforced composites, Int. J. Mech. Sci. 269 (2024) 108989, http://dx.doi.org/10.1016/j.ijmecsci.2024.108989.

[3] L. Mishnaevsky, Repair of wind turbine blades: Review of methods and related computational mechanics problems, Renew. Energy 140 (2019) 828–839, http://dx.doi.org/10.1016/j.renene.2019.03.113.

[4] L. Mishnaevsky, N. Frost-Jensen Johansen, A. Fraisse, S. Fæster, T. Jensen, B. Bendixen, Technologies of wind turbine blade repair: Practical comparison, Energies 15 (5) (2022) 1767, http://dx.doi.org/10.3390/en15051767.

[5] L. Mishnaevsky, Root causes and mechanisms of failure of wind turbine blades: overview, Materials 15 (9) (2022) 2959, http://dx.doi.org/10.3390/ma15092959.

[6] I.L. Hia, V. Vahedi, P. Pasbakhsh, Self-healing polymer composites: prospects, challenges, and applications, Polym. Rev. 56 (2) (2016) 225–261, http://dx.doi.org/10.1080/15583724.2015.1106555.

[7] K. Choi, A. Noh, J. Kim, P.H. Hong, M.J. Ko, S.W. Hong, Properties and applications of self-healing polymeric materials: A review, Polymers 15 (22) (2023) 4408, http://dx.doi.org/10.3390/polym15224408.

[8] P. Wan, S. Wu, Q. Liu, H. Wang, X. Gong, Z. Zhao, S. Xu, J. Jiang, L. Fan, L. Tu, Extrinsic self-healing asphalt materials: A mini review, J. Clean. Prod. 425 (2023) 138910, http://dx.doi.org/10.1016/j.jclepro.2023.138910.

[9] N.N.F. Nik Md Noordin Kahar, A.F. Osman, E. Alosime, N. Arsat, N.A. Mohammad Azman, A. Syamsir, Z. Itam, Z.A. Abdul Hamid, The versatility of polymeric materials as self-healing agents for various types of applications: A review, Polymers 13 (8) (2021) 1194, http://dx.doi.org/10.3390/polym13081194.

[10] B. Li, P.-F. Cao, T. Saito, A.P. Sokolov, Intrinsically self-healing polymers: From mechanistic insight to current challenges, Chem. Rev. 123 (2) (2023) 701–735, http://dx.doi.org/10.1021/acs.chemrev.2c00575.

[11] N.F. Mohd Sani, H.J. Yee, N. Othman, A.A. Talib, R.K. Shuib, Intrinsic self-healing rubber: A review and perspective of material and reinforcement, Polym. Test. 111 (2022) 107598, http://dx.doi.org/10.1016/j.polymertesting.2022.107598.

[12] L. Yuan, S. Huang, A. Gu, G. Liang, F. Chen, Y. Hu, S. Nutt, A cyanate ester/microcapsule system with low cure temperature and self-healing capacity, Compos. Sci. Technol. 87 (2013) 111–117, http://dx.doi.org/10.1016/j.compscitech.2013.08.005.

[13] H. Jin, C.L. Mangun, A.S. Griffin, J.S. Moore, N.R. Sottos, S.R. White, Thermally stable autonomic healing in epoxy using a dual-microcapsule system, Adv. Mater. 26 (2) (2014) 282–287, http://dx.doi.org/10.1002/adma.201470006.

[14] N. El Choufi, S. Mustapha, A. Tehrani B, B.P. Grady, An overview of self-healable polymers and recent advances in the field, Macromol. Rapid Commun. 43 (17) (2022) 2200164, http://dx.doi.org/10.1002/marc.202200164.

[15] Y. Sun, L. Mishnaevsky Jr., Healable polymer blends: Computational analysis of damage and healing mechanisms, Int. J. Mech. Sci. (2025) 109938, http://dx.doi.org/10.1016/j.ijmecsci.2025.109938.

[16] A.M. Peterson, R.E. Jensen, G.R. Palmese, Thermoreversible and remendable glass–polymer interface for fiber-reinforced composites, Compos. Sci. Technol. 71 (5) (2011) 586–592, http://dx.doi.org/10.1016/j.compscitech.2010.11.022.

[17] X. Zhang, S. Liu, Z. He, C. Lei, Self-healing interface of carbon fiber reinforced composites using a thermally reversible sizing agent, Polym. Compos. 42 (9) (2021) 4289–4301, http://dx.doi.org/10.1002/pc.26147.

[18] M. Li, G. Zhao, X. Liu, X. Xie, C. Zhang, H. Yu, X. Jian, Y. Song, J. Xu, Self-healing interface of carbon fiber reinforced composites based on reversible hydrogen-bonded interactions, Compos. Commun. 40 (2023) 101631, http://dx.doi.org/10.1016/j.coco.2023.101631.

[19] D.D.L. Chung, A review of multifunctional polymer-matrix structural composites, Compos. Part B: Eng. 160 (2019) 644–660, http://dx.doi.org/10.1016/j.compositesb.2018.12.117.

[20] X. Luo, R. Ou, D.E. Eberly, A. Singhal, W. Viratyaporn, P.T. Mather, A thermoplastic/thermoset blend exhibiting thermal mending and reversible adhesion, ACS Appl. Mater. Interfaces 1 (3) (2009) 612–620, http://dx.doi.org/10.1021/am8001605.

[21] J. Karger-Kocsis, Self-healing properties of epoxy resins with poly(ε-caprolactone) healing agent, Polym. Bull. 73 (11) (2016) 3081–3093, http://dx.doi.org/10.1007/s00289-016-1642-2.

[22] A. Cohades, E. Manfredi, C.J.G. Plummer, V. Michaud, Thermal mending in immiscible poly(ε-caprolactone)/epoxy blends, Eur. Polym. J. 81 (2016) 114–128, http://dx.doi.org/10.1016/j.eurpolymj.2016.05.026.

[23] L. Simonini, R. Canale, H. Mahmood, A. Dorigato, A. Pegoretti, Multifunctional epoxy/carbon composites with a fully reparable interface, Polym. Compos. 45 (3) (2024) 2558–2568, http://dx.doi.org/10.1002/pc.27939.

[24] Z. Wang, Y. Dong, J.-c. Yang, X.-j. Wang, M.-l. Zhang, G. Zhang, S.-r. Long, S. Liu, J. Yang, Improved interfacial shear strength in carbon fiber enhanced semi-aromatic polyamide 6T composite via in-situ polymerization on fiber surface, Compos. Sci. Technol. 223 (2022) 109401, http://dx.doi.org/10.1016/j.compscitech.2022.109401.

[25] G. Nian, Q. Li, Q. Xu, S. Qu, A cohesive zone model incorporating a Coulomb friction law for fiber-reinforced composites, Compos. Sci. Technol. 157 (2018) 195–201, http://dx.doi.org/10.1016/j.compscitech.2018.01.037.

[26] S. AhmadvashAghbash, I. Verpoest, Y. Swolfs, M. Mehdikhani, Methods and models for fibre–matrix interface characterisation in fibre-reinforced polymers: A review, Int. Mater. Rev. 68 (8) (2023) 1245–1319, http://dx.doi.org/10.1080/09506608.2023.2265701.

[27] B. Miller, P. Muri, L. Rebenfeld, A microbond method for determination of the shear strength of a fiber/resin interface, Compos. Sci. Technol. 28 (1) (1987) 17–32, http://dx.doi.org/10.1016/0266-3538(87)90059-5.

[28] R. Dsouza, P. Antunes, M. Kakkonen, J. Jokinen, E. Sarlin, P. Kallio, M. Kanerva, 3D interfacial debonding during microbond testing: Advantages of local strain recording, Compos. Sci. Technol. 195 (2020) 108163, http://dx.doi.org/10.1016/j.compscitech.2020.108163.

[29] R. Dsouza, M. Kakkonen, A. Prapavesis, E. Sarlin, P. Antunes, A.W. Van Vuure, P. Kallio, M. Kanerva, Does a polymer film due to Rayleigh-instability affect interfacial properties measured by microbond test? Compos. Interfaces (2024) 1–27, http://dx.doi.org/10.1080/09276440.2024.2379637.

[30] R.D. Dsouza, D. Di Vito, J. Jokinen, M. Kanerva, Mutual dependence of experimental and data analysis features in characterization of fiber-matrix interface via microdroplets, Polym. Compos. 44 (11) (2023) 7611–7630, http://dx.doi.org/10.1002/pc.27649.

[31] R. Li, Z. Xu, X. Zou, X. He, Modeling the progressive damage of cryogenic microdroplet tests using a temperature-friction cohesive zone model, Polym. Compos. 45 (3) (2024) 2156–2170, http://dx.doi.org/10.1002/pc.27910.

[32] M. Yuan, H. Zhao, S. Liu, H. Ren, B. Zhang, X. Sun, J. Chen, Determination of cohesive parameters for fibre-reinforced composite interfaces based on finite element analysis and machine learning, J. Compos. Mater. 56 (27) (2022) 4113–4122, http://dx.doi.org/10.1177/00219983221127400.

[33] R. Li, Z. Xu, X. Zou, C. Hu, X. He, A frictional cohesive zone model for characterizing transverse compression responses of unidirectional fiber-reinforced polymer composites, Mech. Adv. Mater. Struct. 30 (11) (2023) 2164–2172, http://dx.doi.org/10.1080/15376494.2022.2051103.

[34] P. Laurikainen, R. Dsouza, M. Kakkonen, M. Kanerva, E. Sarlin, Exploring the role of fibre sizing to the fatigue of glass fibre composites using a novel, reliable micro-fatigue test, Compos. Part A: Appl. Sci. Manuf. 167 (2023) 107425, http://dx.doi.org/10.1016/j.compositesa.2023.107425.

[35] S. AhmadvashAghbash, C. Breite, M. Mehdikhani, Y. Swolfs, Longitudinal debonding in unidirectional fibre-reinforced composites: Numerical analysis of the effect of interfacial properties, Compos. Sci. Technol. 218 (2022) 109117, http://dx.doi.org/10.1016/j.compscitech.2021.109117.

[36] L. Simonini, M. Kakkonen, R. Dsouza, M. Kanerva, H. Mahmood, A. Dorigato, A. Pegoretti, Tailoring the interfacial properties of glass fiber-epoxy microcomposites through the development of a self-healing poly(ε-caprolactone) coating, Compos. Sci. Technol. 261 (2025) 110991, http://dx.doi.org/10.1016/j.compscitech.2024.110991.

[37] S. Joncas, Thermoplastic Composite Wind Turbine Blades: an Integrated Design Approach (Ph.D. thesis), Delft University of Technology, 2010.

[38] L. Mishnaevsky, K. Branner, H.N. Petersen, J. Beauson, M. McGugan, B.F. Sørensen, Materials for wind turbine blades: An overview, Materials 10 (11) (2017) 1285, http://dx.doi.org/10.3390/ma10111285.

[39] W. Badri, K. Miladi, Q.A. Nazari, H. Fessi, A. Elaissari, Effect of process and formulation parameters on polycaprolactone nanoparticles prepared by solvent displacement, Colloids Surfaces A: Physicochem. Eng. Asp. 516 (2017) 238–244, http://dx.doi.org/10.1016/j.colsurfa.2016.12.029.

[40] N.K. Singh, B.D. Purkayastha, J.K. Roy, R.M. Banik, M. Yashpal, G. Singh, S. Malik, P. Maiti, Nanoparticle-induced controlled biodegradation and its mechanism in poly(ε-caprolactone), ACS Appl. Mater. Interfaces 2 (1) (2010) 69–81, http://dx.doi.org/10.1021/am900584r.

[41] G. Quino, J. Gargiuli, S. Pimenta, I. Hamerton, P. Robinson, R.S. Trask, Experimental characterisation of the dilation angle of polymers, Polym. Test. 125 (2023) 108137, http://dx.doi.org/10.1016/j.polymertesting.2023.108137.

[42] P.S. Theocaris, E. Koroneos, The friction angle in plasticized epoxy polymers during polymerization, Rheol. Acta 14 (8) (1975) 745–752, http://dx.doi.org/10.1007/BF01515934.

[43] S. Sockalingam, M. Dey, J.W. Gillespie, M. Keefe, Finite element analysis of the microdroplet test method using cohesive zone model of the fiber/matrix interface, Compos. Part A: Appl. Sci. Manuf. 56 (2014) 239–247, http://dx.doi.org/10.1016/j.compositesa.2013.10.021.

[44] T. Schüller, W. Beckert, B. Lauke, A finite element model to include interfacial roughness into simulations of micromechanical tests, Comput. Mater. Sci. 15 (3) (1999) 357–366, http://dx.doi.org/10.1016/S0927-0256(99)00028-2.

[45] Abaqus Documentation, SIMULIA user assistance, dassault systems simulia corporation, 2023, URL https://help.3ds.com.

[46] P.D. Jero, R.J. Kerans, T.A. Parthasarathy, Effect of interfacial roughness on the frictional stress measured using pushout tests, J. Am. Ceram. Soc. 74 (11) (1991) 2793–2801, http://dx.doi.org/10.1111/j.1151-2916.1991.tb06845.x.

[47] T.A. Parthasarathy, D.B. Marshall, R.J. Kerans, Analysis of the effect of interfacial roughness on fiber debonding and sliding in brittle matrix composites, Acta Met. et Mater. 42 (11) (1994) 3773–3784, http://dx.doi.org/10.1016/0956-7151(94)90443-X.

[48] B.F. Sørensen, S. Goutianos, Mixed Mode cohesive law with interface dilatation, Mech. Mater. 70 (2014) 76–93, http://dx.doi.org/10.1016/j.mechmat.2013.11.006.

[49] H. Song, R.J. Dikken, L. Nicola, E. Van der Giessen, Plastic ploughing of a sinusoidal asperity on a rough surface, J. Appl. Mech. 82 (071006) (2015) http://dx.doi.org/10.1115/1.4030318.

[50] D.B. Marshall, M.C. Shaw, W.L. Morris, Measurement of interfacial debonding and sliding resistance in fiber reinforced intermetallics, Acta Met. et Mater. 40 (3) (1992) 443–454, http://dx.doi.org/10.1016/0956-7151(92)90392-R.

[51] F.P. Incropera, D.P. DeWitt, T.L. Bergman, A.S. Lavine (Eds.), Principles of Heat and Mass Transfer, 7. ed., international student version, Wiley, Hoboken, NJ, 2013.

[52] Q. Guo, G. Groeninckx, Crystallization kinetics of poly(ε-caprolactone) in miscible thermosetting polymer blends of epoxy resin and poly(ε-caprolactone), Polymer 42 (21) (2001) 8647–8655, http://dx.doi.org/10.1016/S0032-3861(01)00348-2.

[53] M. Avrami, Kinetics of phase change. I general theory, J. Chem. Phys. 7 (12) (1939) 1103–1112, http://dx.doi.org/10.1063/1.1750380.

[54] M. Avrami, Kinetics of phase change. II transformation-time relations for random distribution of nuclei, J. Chem. Phys. 8 (2) (1940) 212–224, http://dx.doi.org/10.1063/1.1750631.

[55] M. Avrami, Granulation, phase change, and microstructure kinetics of phase change. III, J. Chem. Phys. 9 (2) (1941) 177–184, http://dx.doi.org/10.1063/1.1750872.

[56] K. Nie, W. Pang, S. Zheng, Y. Wang, F. Lu, Q. Zhu, Non-isothermal crystallization kinetics of poly(ε-caprolactone) in hydrogen-bond-coupled polymeric-inorganic hybrid materials, Polym. Int. 54 (2) (2005) 327–335, http://dx.doi.org/10.1002/pi.1682.

[57] S.E. Asmai, F. Hennebelle, T. Coorevits, J.-F. Fontaine, Determination of the coefficient of expansion of a carbon tube and its assembly for thermal compensation of metrological structures, in: 19th International Congress of Metrology (CIM2019), EDP Sciences, 2019, p. 26003, http://dx.doi.org/10.1051/metrology/201926003.

[58] X. Liu, H. Dong, Y. Li, N. Mei, Thermal conductivity and Raman spectra of carbon fibers, Int. J. Thermophys. 38 (10) (2017) 150, http://dx.doi.org/10.1007/s10765-017-2275-x.

[59] H. Tian, F. Wu, P. Chen, X. Peng, H. Fang, Microwave-assisted in situ polymerization of polycaprolactone/boron nitride composites with enhanced thermal conductivity and mechanical properties, Polym. Int. 69 (7) (2020) 635–643, http://dx.doi.org/10.1002/pi.6000.

[60] A.M. Ali, M.A. Jaber, T.N. A., Mechanical and thermal properties of polyurethane/epoxy IPN's, J. Sci. Eng. Res. 7 (5) (2020) 16–19.

[61] I.A. Popov, O.L. Hamidullin, L.M. Amirova, I.A. Popov, Research of the thermophysical properties of CFRP with different reinforcements by methods of a stationary heat flow and differential scanning calorimeter with temperature modulation, Tepl. Vysok. Temp. 61 (5) (2023) 706–713, http://dx.doi.org/10.31857/S0040364423050137.

[62] P. Skoglund, Å. Fransson, Continuous cooling and isothermal crystallization of polycaprolactone, J. Appl. Polym. Sci. 61 (13) (1996) 2455–2465.

[63] X. Qiao, W. Li, K. Sun, S. Xu, X. Chen, Isothermal crystallization kinetics of silk fibroin fiber-reinforced poly(ε-caprolactone) biocomposites, Polym. Int. 58 (5) (2009) 530–537, http://dx.doi.org/10.1002/pi.2563.

[64] C. Leistner, M. Löffelholz, S. Hartmann, Model validation of polymer curing processes using thermography, Polym. Test. 77 (2019) 105893, http://dx.doi.org/10.1016/j.polymertesting.2019.05.009.

[65] A.P. Kotula, C.R. Snyder, K.B. Migler, Determining conformational order and crystallinity in polycaprolactone via Raman spectroscopy, Polymer 117 (2017) 1–10, http://dx.doi.org/10.1016/j.polymer.2017.04.006.

[66] H. Bai, R. Bai, T. Zhao, Z. Lei, X. Hong, C. Liu, T. Wang, Characterization of interfacial bonding properties of Vitrimer resin/ T700 fibre, Compos. Interfaces 30 (2) (2023) 163–185, http://dx.doi.org/10.1080/09276440.2022.2076365.

[67] N. Coburn, P. Douglas, D. Kaya, J. Gupta, T. McNally, Isothermal and non-isothermal crystallization kinetics of composites of poly(propylene) and MWCNTs, Adv. Ind. Eng. Polym. Res. 1 (1) (2018) 99–110, http://dx.doi.org/10.1016/j.aiepr.2018.06.001.

[68] Z.-H. Gao, H.-J. Gao, Y.-D. Zhang, Q. Wu, Experiment and mechanism investigation on the effect of heat treatment on residual stress and mechanical properties of SiCp/Al–Cu–Mg composites, Mater. Sci. Eng.: A 884 (2023) 145555, http://dx.doi.org/10.1016/j.msea.2023.145555.

[69] C.T. Chou, U. Gaur, B. Miller, The effect of microvise gap width on microbond pull-out test results, Compos. Sci. Technol. 51 (1) (1994) 111–116, http://dx.doi.org/10.1016/0266-3538(94)90161-9.

[70] C. Zhi, H. Long, M. Miao, Influence of microbond test parameters on interfacial shear strength of fiber reinforced polymer-matrix composites, Compos. Part A: Appl. Sci. Manuf. 100 (2017) 55–63, http://dx.doi.org/10.1016/j.compositesa.2017.05.004.

[71] B. Miller, U. Gaur, D.E. Hirt, Measurement and mechanical aspects of the microbond pull-out technique for obtaining fiber/resin interfacial shear strength, Compos. Sci. Technol. 42 (1) (1991) 207–219, http://dx.doi.org/10.1016/0266-3538(91)90018-K.

[72] N.-S. Choi, J.-E. Park, Fiber/matrix interfacial shear strength measured by a quasi-disk microbond specimen, Compos. Sci. Technol. 69 (10) (2009) 1615–1622, http://dx.doi.org/10.1016/j.compscitech.2009.03.012.

[73] B. Morlin, L.M. Vas, T. Czigany, Investigation of fiber/matrix adhesion: Test speed and specimen shape effects in the cylinder test, J. Mater. Sci. 48 (8) (2013) 3185–3191, http://dx.doi.org/10.1007/s10853-012-7097-4.